Supplementary Information

Decoupled Zn-Sr-Nd isotopes of continental intraplate basalts caused by two-stage melting process

Rong Xu[1,2], Yongsheng Liu[2]*, Sarah Lambart[3], Kaj Hoernle[4,5], Yangtao Zhu[2], Zongqi Zou[2], Junbo Zhang[2], Zaicong Wang[2], Ming Li[2], Frédéric Moynier[6], Keqing Zong[2], Haihong Chen[2], Zhaochu Hu[2]

[1]State Key Laboratory of Ore Deposit Geochemistry, Institute of Geochemistry, Chinese Academy of Sciences, Guiyang 550081, China

[2]State Key Laboratory of Geological Processes and Mineral Resources, School of Earth Sciences, China University of Geosciences, Wuhan 430074, China

[3]Geology and Geophysics, University of Utah, Salt Lake City, Utah, United States

[4]GEOMAR Helmholtz Centre for Ocean Research Kiel, 24148 Kiel, Germany

[5]Kiel University, Institute of Geosciences, 24118 Kiel, Germany

[6]Université de Paris, Institut de Physique du Globe de Paris, CNRS UMR 7154, 75238 Paris Cedex 05, France

E-mail: rongxu@cug.edu.cn; yshliu@cug.edu.cn; sarahlambart@utah.edu

This file includes:

(1) Research Data Statement

All unpublished research data used in this manuscript are included in Tables S1-S7, which have already been uploaded in this submission.

Description of Research Data Files

File Name: Table S1: Major element compositions of the Zhejiang basalts (wt.%).

File Name: Table S2: Trace element compositions of the Zhejiang basalts (ppm).

File Name: Table S3: Sr-Nd isotopic compositions of the Zhejiang basalts.

File Name: Table S4: Zinc isotopic compositions of the Zhejiang basalts.

File Name: Table S5: Trace element compositions of the standard materials (ppm).

File Name: Table S6: Sr-Nd isotopic compositions of standard materials.

File Name: Table S7: Zinc isotopic compositions of the reference materials.

(2) Supplementary Figures 1-10

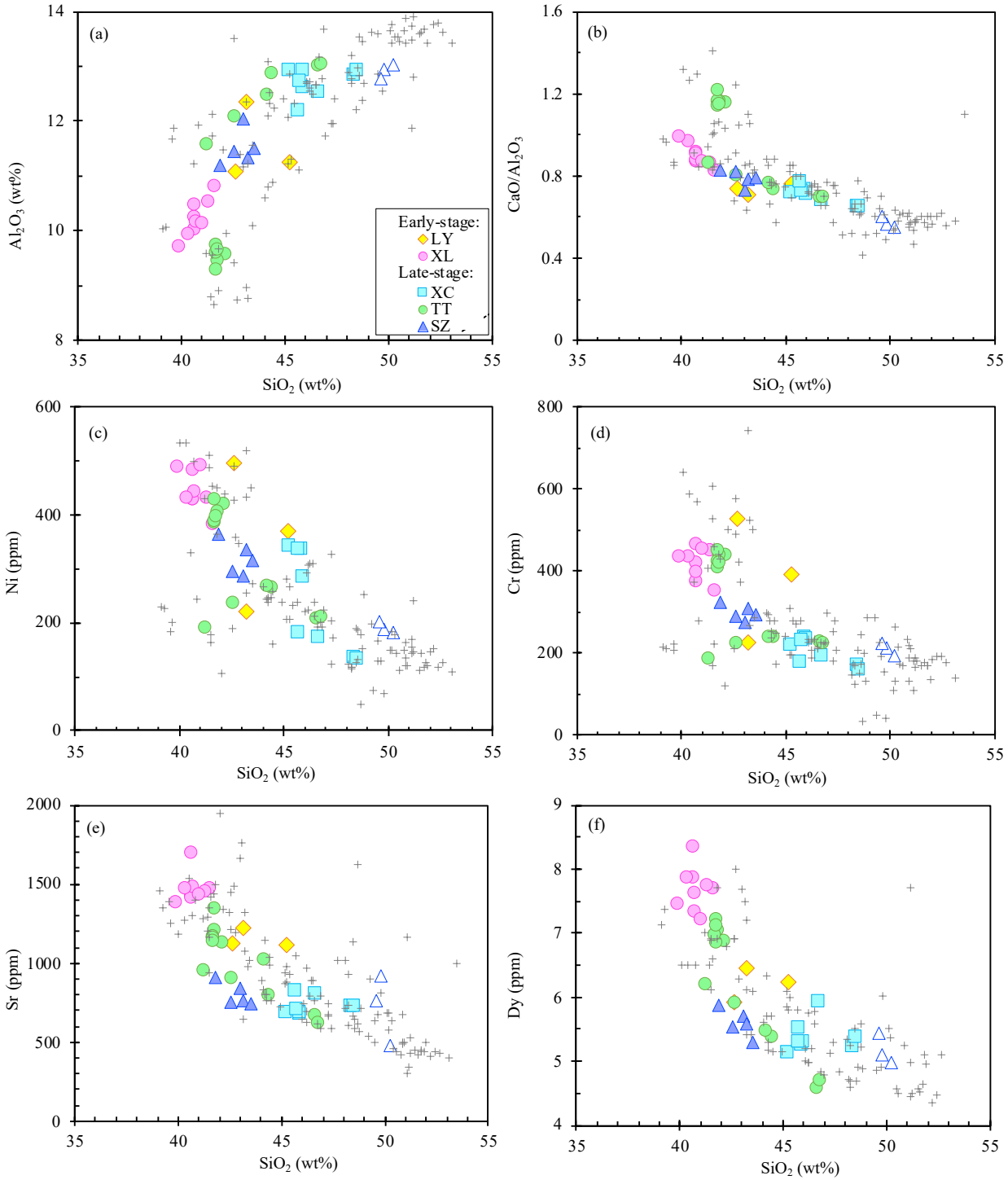

Fig. S1. Al_2O_3, CaO/Al_2O_3, Ni, Cr, Sr, and Dy versus SiO_2 for the studied samples. Error bars are smaller than the symbols. Our samples are from Xilong (XL) and Longyou (LY) in the inland area, and from Xinchang (XC), Shengzhou (SZ) and Tiantai (TT) in the coastal area. Open triangles show the crustal contaminated samples from SZ (see text for details). The grey crosses are published data for Zhejiang basalts (Ho et al., 2003; Huang et al., 2015; Li et al., 2015; Liu et al., 2016; Yu et al., 2015; Zou et al., 2000). Symbols are the same as in Figure 2.

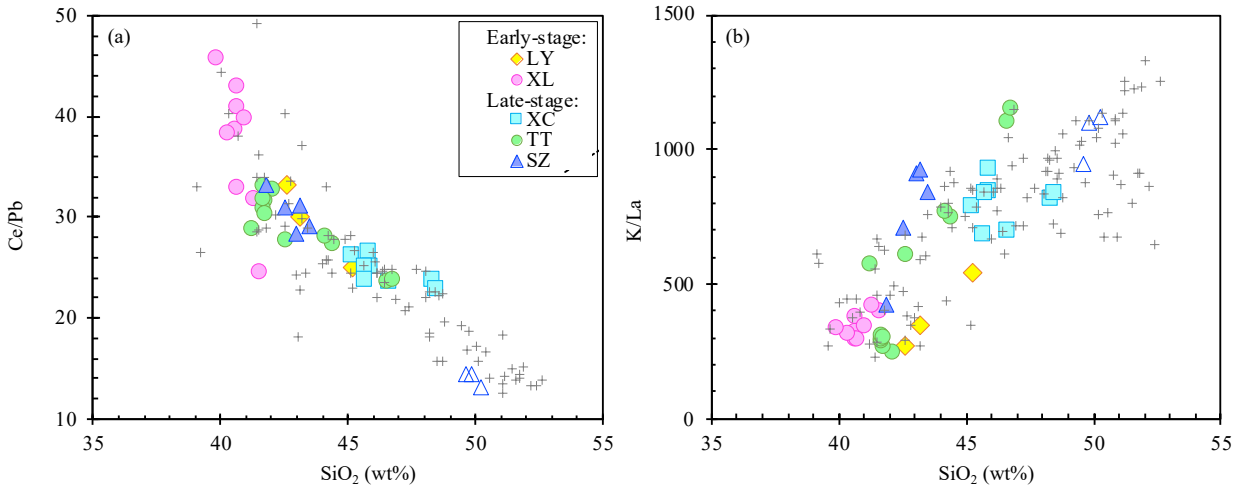

Fig. S2. (a) Ce/Pb and (b) K/La versus SiO_2 for the studied samples. Symbols are the same as in Figure 2.

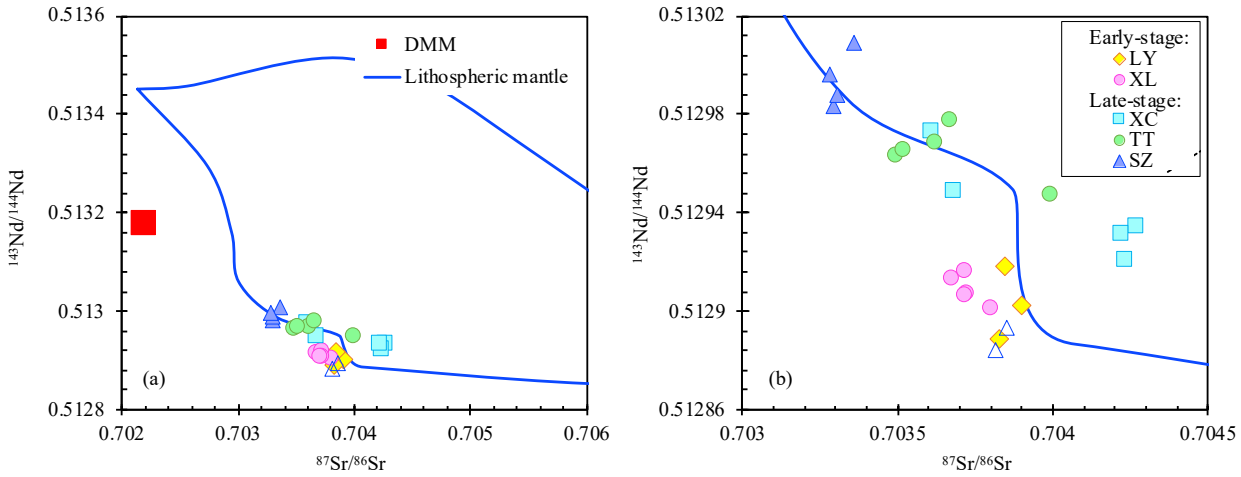

Fig. S3. (a) Comparison of the studied basalts with lithospheric peridotite mantle xenoliths from South China and depleted MORB mantle (DMM) in the $^{143}Nd/^{144}Nd$ versus $^{87}Sr/^{86}Sr$ diagram. Data source: lithospheric mantle xenoliths (Tatsumoto et al., 1992; Qi et al., 1995) and DMM (Workman and Hart, 2005). (b) Enlargement of (a).

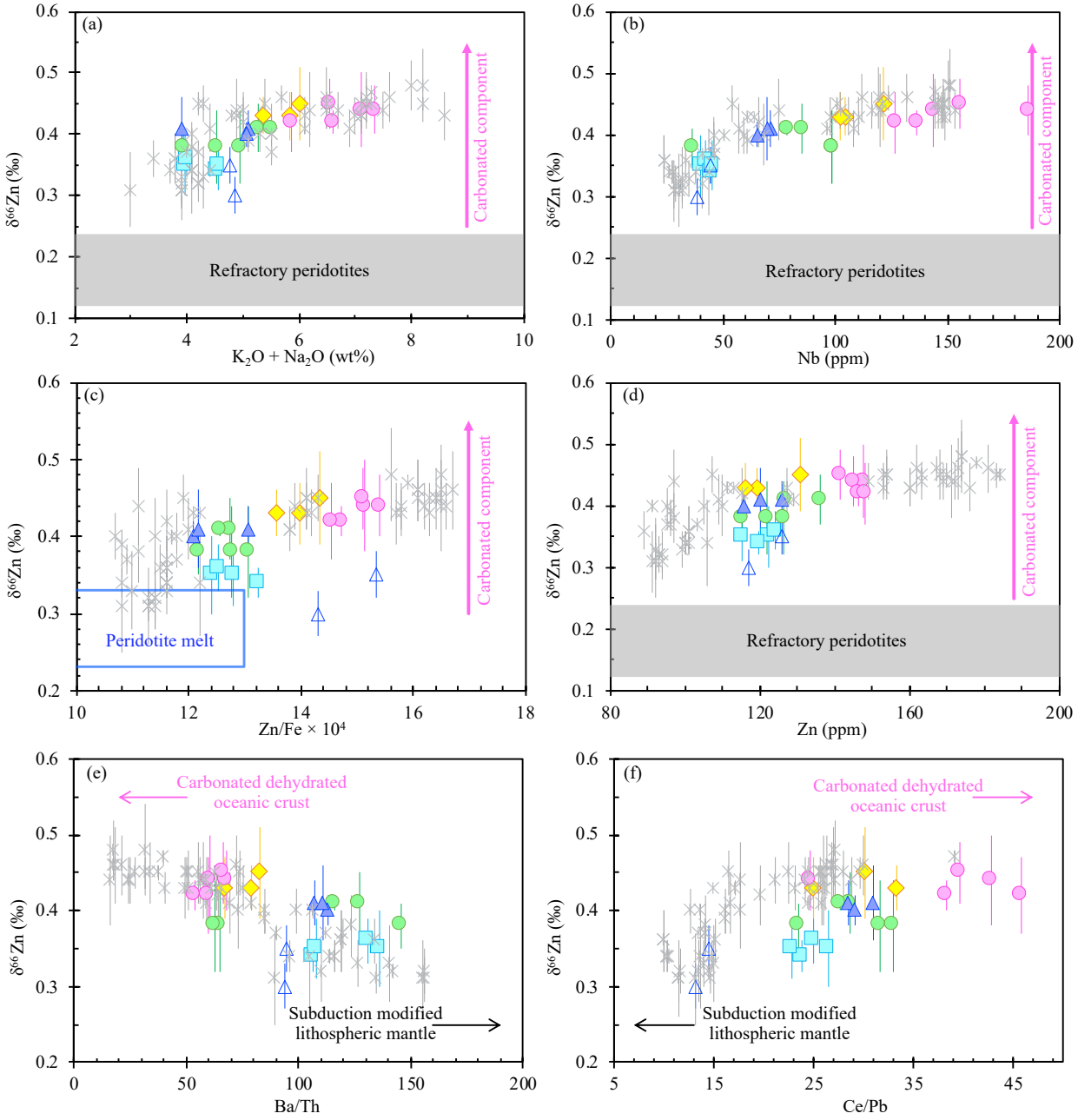

Fig. S4. Variations of δ^{66}Zn with (a) total alkali, (b) Nb, (c) Zn/Fe, (d) Zn, (e) Ba/Th and (f) Ce/Pb. Data for alkali basalts from Shandong, North China craton (grey cross symbols) are from Wang et al. (2018). Data source for δ^{66}Zn of refractory peridotites is in Wang et al. (2018). Zn/Fe ranges for melts of peridotites and pyroxenites can be found in Le Roux et al. (2010). In (a-d), the pink arrows indicate increasing contribution from the carbonated component. In (e-f), the black arrows show the effect of increasing of contribution from lithospheric mantle. Symbols are the same as in Fig. 2.

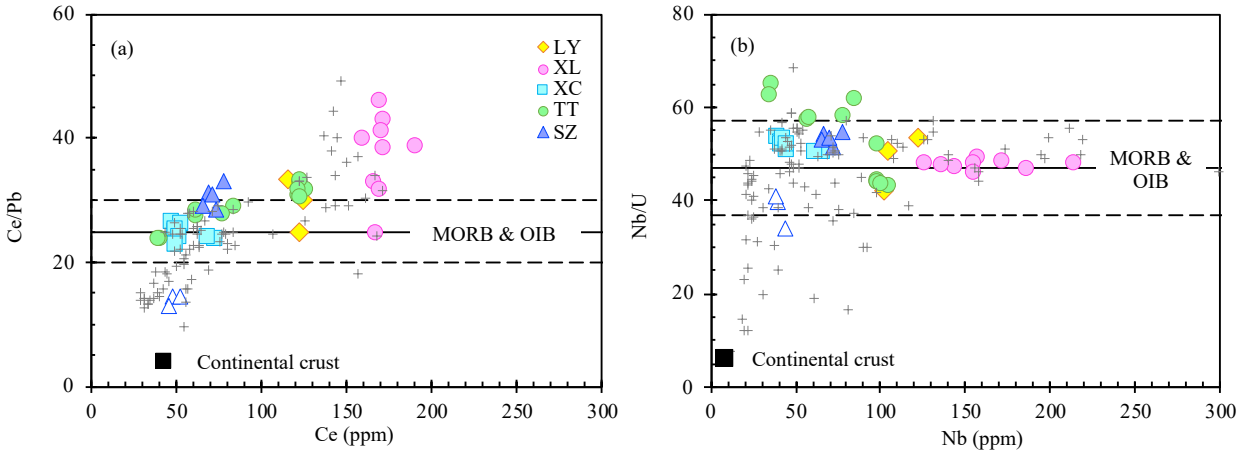

Fig. S5. (a) Ce/Pb versus Ce and (b) Nb/U versus Nb for the studied samples. Symbols are the same as in Figure S1. Errors bars are smaller than the symbols. Also shown for reference are the composition of the continental crust from Rudnick and Gao (2003) and ratios for oceanic basalts (MORB and OIB) with averages of Nb/U and Ce/Pb of 47 ± 7(1σ) and 25 ± 5(1σ), respectively (Hofmann et al., 1986).

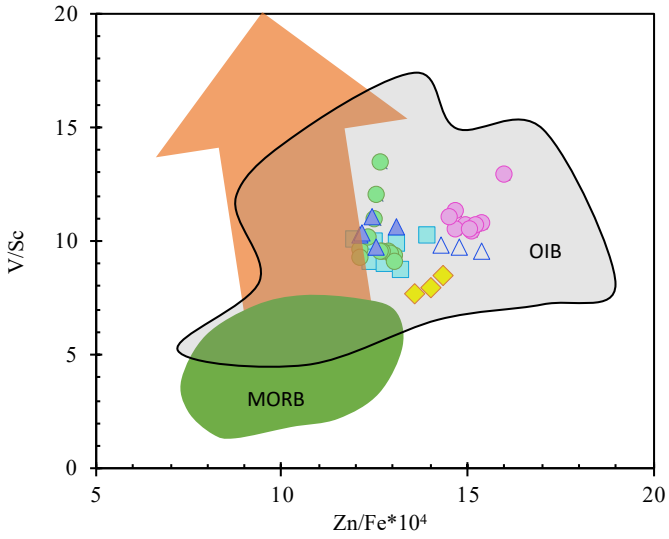

Fig. S6. V/Sc vs. Zn/Fe*10^4 for the studied samples. The green field and the grey field are the range of MORB and primitive OIB with MgO > 10%. The orange arrow shows the expected effect of increasing oxygen fugacity during mantle melting. Modified after Davis et al. (2013).

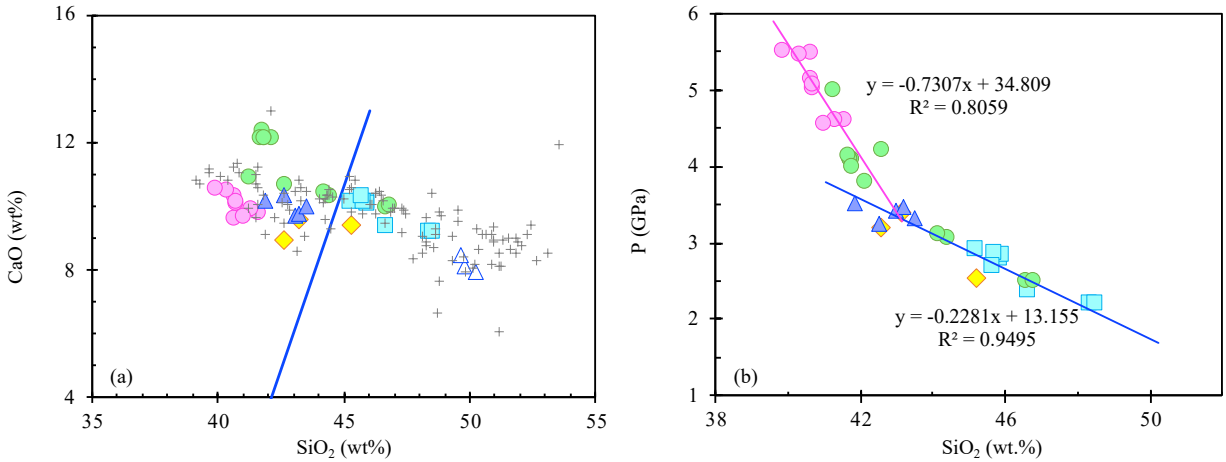

Fig. S7. (a) CaO versus SiO_2 for the studied samples. The blue line is an approximate filter that separates CO_2-bearing (left side) and CO_2-free (right side) basalts (Herzberg and Asimow, 2008). (b) SiO_2 versus pressure calculated with Lee et al. (2009). The blue and pink lines are the linear regressions for samples with and without CO_2 defined in (a), respectively. Symbols are the same as in Fig. 2.

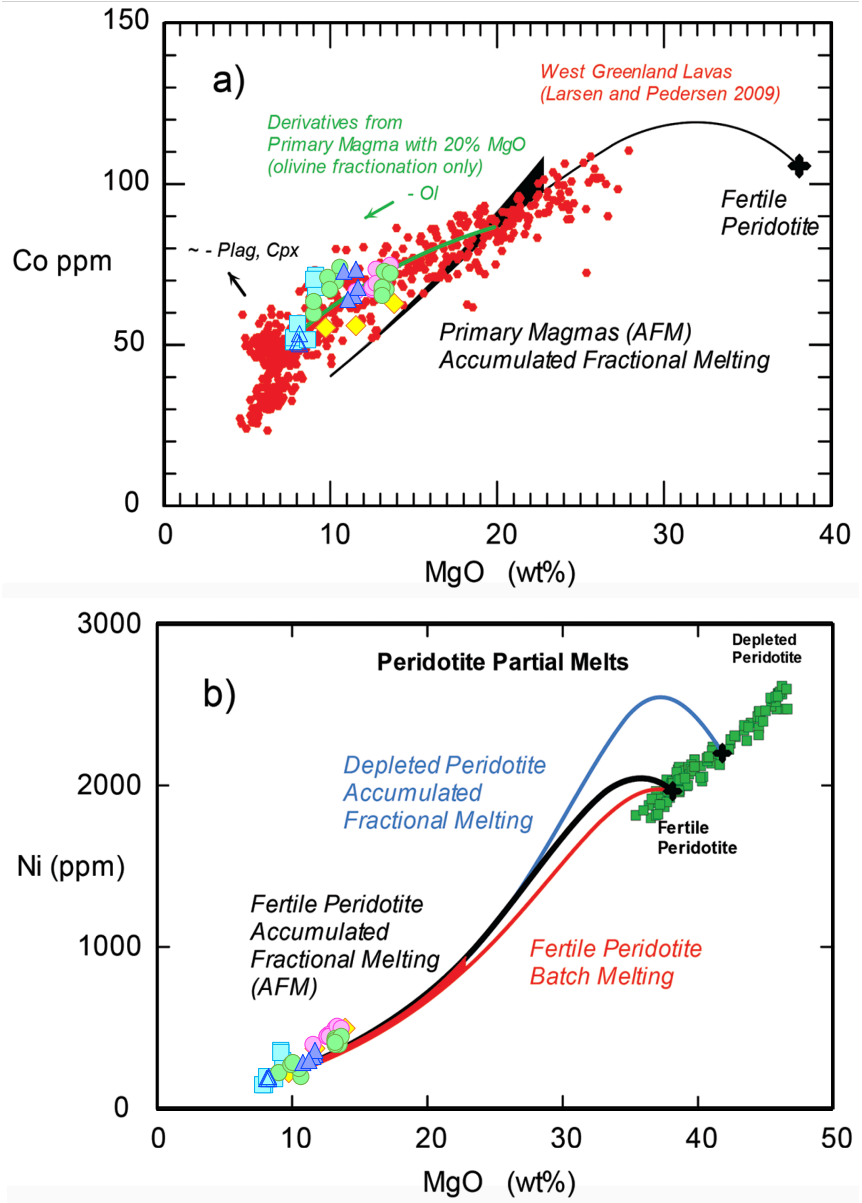

Fig. S8. Co and Ni contents vs. MgO for the studied samples. Modified after Herzberg et al. (2016).

Fig. S9

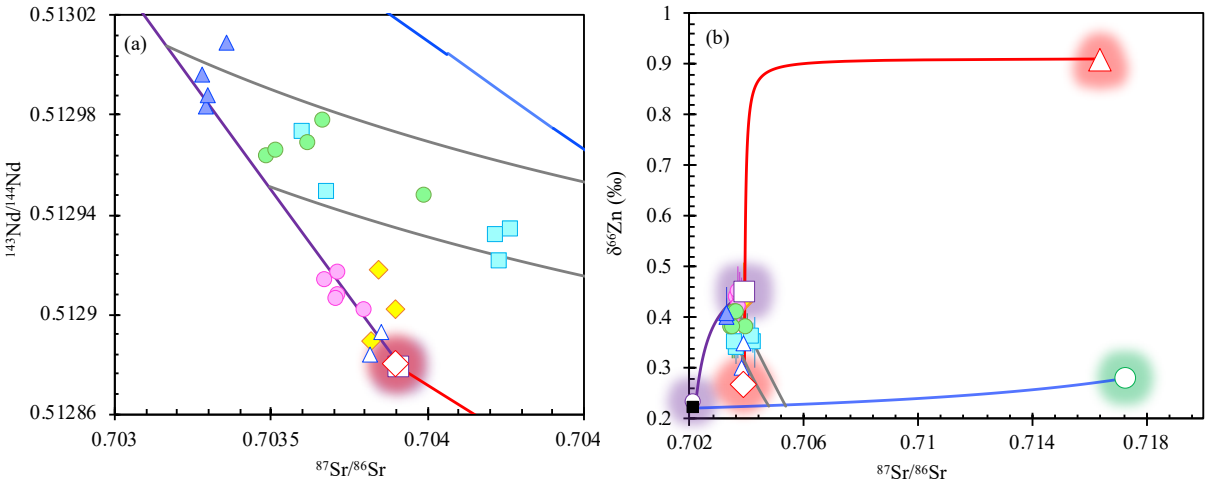

Fig. S9. (a) Enlargement of Fig. 5a ($^{143}Nd/^{144}Nd$ versus $^{87}Sr/^{86}Sr$ diagram) in the main text. (b) The complete Fig. 5b ($\delta^{66}Zn$ versus $^{87}Sr/^{86}Sr$ diagram) in the main text showing all the end members including GLOSS and carbonate sediments.

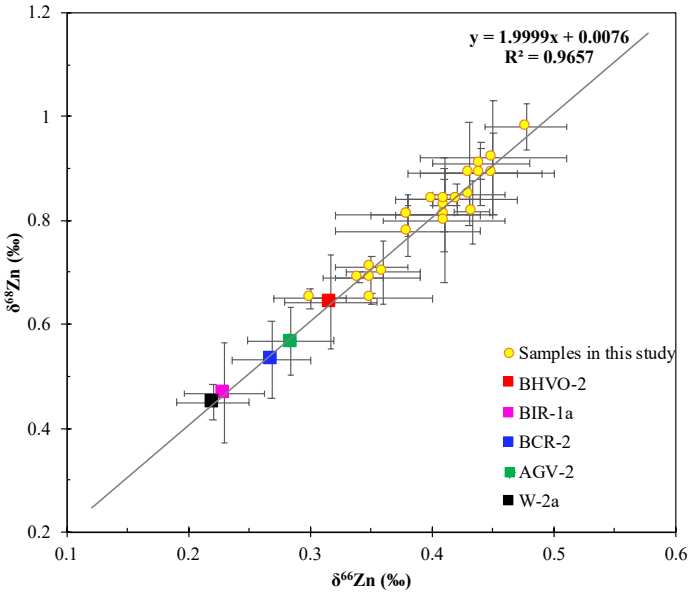

Fig. S10. Relationship between measured $\delta^{66}Zn$ and $\delta^{68}Zn$ values for Zhejiang and standard materials.

References

Davis, F.A., Humayun, M., Hirschmann, M.M., Cooper, R.S., 2013. Experimentally determined mineral/melt partitioning of first-row transition elements (FRTE) during partial melting of peridotite at 3GPa. Geochimica et Cosmochimica Acta 104 232-260.

Herzberg, C., Asimow, P.D., 2008. Petrology of some oceanic island basalts: PRIMELT2. XLS software for primary magma calculation. Geochemistry, Geophysics, Geosystems 9 (9).

Herzberg, C., Vidito, C., Starkey, N.A., 2016. Nickel–cobalt contents of olivine record origins of mantle peridotite and related rocks. American Mineralogist 101 (9) 1952-1966.

Ho, K.-S., Chen, J.-C., Lo, C.-H., Zhao, H.-L., 2003. 40Ar–39Ar dating and geochemical characteristics of late Cenozoic basaltic rocks from the Zhejiang–Fujian region, SE China: eruption ages, magma evolution and petrogenesis. Chemical Geology 197 (1-4) 287-318.

Hofmann, A.W., Jochum, K.P., Seufert, M., White, W.M., 1986. Nb and Pb in oceanic basalts: new constraints on mantle evolution. Earth and Planetary Science Letters 79 (1) 33-45.

Huang, J., Li, S.-G., Xiao, Y., Ke, S., Li, W.-Y., Tian, Y., 2015. Origin of low δ26Mg Cenozoic basalts from South China Block and their geodynamic implications. Geochimica et Cosmochimica Acta 164 298-317.

Le Roux, V., Lee, C.T., Turner, S.J., 2010. Zn/Fe systematics in mafic and ultramafic systems: Implications for detecting major element heterogeneities in the Earth's mantle. Geochimica et Cosmochimica Acta 74 (9) 2779-2796.

Lee, C.-T.A., Luffi, P., Plank, T., Dalton, H., Leeman, W.P., 2009. Constraints on the depths and temperatures of basaltic magma generation on Earth and other terrestrial planets using new thermobarometers for mafic magmas. Earth and Planetary Science Letters 279 (1-2) 20-33.

Li, Y.-Q., Ma, C.-Q., Robinson, P.T., Zhou, Q., Liu, M.-L., 2015. Recycling of oceanic crust from a stagnant slab in the mantle transition zone: Evidence from Cenozoic continental basalts in Zhejiang Province, SE China. Lithos 230 146-165.

Liu, S.-C., Xia, Q.-K., Choi, S.H., Deloule, E., Li, P., Liu, J., 2016. Continuous supply of recycled Pacific oceanic materials in the source of Cenozoic basalts in SE China: the Zhejiang case. Contributions to Mineralogy and Petrology 171 (12).

Qi, Q.U., Taylor, L.A., Zhou, X., 1995. Petrology and Geochemistry of Mantle Peridotite Xenoliths from SE China. Journal of Petrology 36 (1) 55-79.

Rudnick, R.L., Gao, S., 2003. Composition of the continental crust. Treatise on geochemistry 3 1-64.

Tatsumoto, M., Basu, A.R., Wankang, H., Junwen, W., Guanghong, X., 1992. Sr, Nd, and Pb isotopes of ultramafic xenoliths in volcanic rocks of Eastern China: enriched components EMI and EMII in subcontinental lithosphere. Earth and Planetary Science Letters 113 (1) 107-128.

Wang, Z.-Z., Liu, S.-A., Chen, L.-H., Li, S.-G., Zeng, G., 2018. Compositional transition in natural alkaline lavas through silica-undersaturated melt–lithosphere interaction. Geology 46 (9) 771-774.

Workman, R.K., Hart, S.R., 2005. Major and trace element composition of the depleted MORB mantle (DMM). Earth and Planetary Science Letters 231 (1-2) 53-72.

Yu, X., Chen, L.-H., Zeng, G., 2015. Growing magma chambers control the distribution of small-scale flood basalts. Scientific reports 5.

Zou, H., Zindler, A., Xu, X., Qi, Q., 2000. Major, trace element, and Nd, Sr and Pb isotope studies of Cenozoic basalts in SE China: mantle sources, regional variations, and tectonic significance. Chemical Geology 171 (1) 33-47.

(3) Supplementary Text S1_Methods

Major element analyses

Whole-rock major elements were determined at the Wuhan Sample Solution Analytical Technology Co., Ltd., Wuhan, China. Major element concentrations were determined by a Rigaku-3080 X-ray fluorescence (XRF) employing a Rh-anode X-ray tube with a voltage of 40 kV and a current of 70 mA after samples were fused in a high-frequency melting furnace. The analytical precision (relative standard deviation, RSD) and accuracy (relative error, RE) are both better than 4% for the major element concentrations determined during this study, and further details of the analytical procedures used are given in Ma et al. (2012).

Trace element analyses

Trace-element concentrations of whole-rock samples were determined by ICP-MS (Agilent 7500a with shielded torch) after acid digestion of the samples in high-pressure Teflon bombs. Sample powder (200 mesh) was weighed into a Teflon bomb and moistened with a few drops of Milli-Q ultrapure water. Then, 1.5 ml of HNO3 and 1.5 ml of HF were added to the Teflon bomb, which was sealed in a steel jacket and heated in an oven at 190 °C for 48 h to completely dissolve the sample. After opening the bomb and evaporating the solution on a hotplate at ~115 °C to dryness, 1 ml of HNO3 was added to the Teflon bomb and evaporated to a second round of dryness. The resultant salt was redissolved by adding ~3 ml of 30% HNO3, resealed in a steel jacket and heated in an oven at 190 °C for 12–24 h. The final solution was diluted to ~100 g with a mixture of 2%HNO3 for ICP-MS analysis. Analyses of international rock standards (AGV-2, BHVO-1, BHVO-2, GSR-1, GSR-3 and BCR-2) indicate that the precision and accuracy are better than 5% for most elements and ~10% for some transitional elements (Table S5). The detailed sample-digestion procedure for ICP-MS analyses and the analytical precision and accuracy for trace

elements have been described by Liu et al. (2008).

Whole-rock Sr–Nd isotopes

Whole-rock Sr–Nd isotopic compositions were determined using a Triton Tl mass spectrometer operated in static mode at the Wuhan Sample Solution Analytical Technology Co., Ltd., Wuhan, China, yielding an analytical precision better than 0.002%. Prior to analysis, ~100 mg of sample material was dissolved in HF + HNO_3 acid in Teflon bombs at ~195°C for two days. $^{87}Rb/^{86}Sr$ and $^{147}Sm/^{144}Nd$ ratios were calculated using measured whole-rock Rb, Sr, Sm, and Nd concentrations determined by ICP–MS. The resulting measured $^{143}Nd/^{144}Nd$ and $^{87}Sr/^{86}Sr$ ratios were normalized to $^{146}Nd/^{144}Nd = 0.7219$ and $^{86}Sr/^{88}Sr = 0.1194$, respectively. Comparison between our results of Sr-Nd standard and preferred values are summarized in Table S6. Full details of the Rb–Sr and Sm–Nd procedures used during this study given in Gao et al. (2004).

Zinc isotopes

Zinc isotopic were measured at the State Key Laboratory of Geological Processes and Mineral Resources, China University of Geosciences (Wuhan). Approximately 10-40 mg (containing ~1μg Zn) of powder of sample are mixed with 1ml of concentrated HF and 1ml of concentrated HNO_3 to be dissolved on hotplate at 120℃ for 24h. And then the solutions are dried down and an additional 1ml of concentrated HNO_3 is added and evaporated to ensure removal of most of the HF. Afterwards, aqua regia (1.5ml of concentrated HCl + 0.5ml of concentrated HNO_3) is added to the sample and the beaker put on a hotplate at 120℃ for 48h to digest the residues including fluorides. After complete digestion, an additional 1ml of concentrated HCl is added and evaporated to dryness. Finally, the residual sample is dissolved in 1ml of 8 mol/L HCl + 0.001% H_2O_2 to

prepare for chemical purification. The chemical purification is described by Zhu et al. (2019) which is a protocol adapted from Maréchal et al. (1999) and Liu et al. (2014). The sample solution was loaded on 2ml pre-cleaned AG-MP-1M resin. After the elution of matrix elements (e.g., K, Na, Mg, Cu, Fe, etc.) in 8 mol/L HCl + 0.001% H_2O_2 and 0.5 mol/L HCl, Zn is collected by adding an additional 10 ml 0.5 mol/L HNO_3. The final Zn elution is dried down and dissolved in 2% (m/m) HNO_3 for analysis.

Zinc isotopic ratios were measured on a Nu Plasma 1700 MC-ICP-MS instrument located at the State Key Laboratory of Geological Processes and Mineral Resources, China University of Geosciences (Wuhan). The instrumental isotopic fractionation is corrected by the sample-standard bracketing method and by adding Cu as an internal standard (Maréchal et al., 1999). The bracketing standard is NIST SRM 683, which is fractionated compared to JMC Lyon by 0.12 ± 0.04‰ (Chen et al., 2016). The Zn concentrations of the samples were checked and adjusted to match the NIST SRM 683 solution within 10%. Zinc solutions were introduced to the Ar plasma using a Glass Expansion nebulizer with an uptake rate of ~100 µl/min.

In total, the intensity of seven signals (^{60}Ni, ^{63}Cu, ^{64}Zn, ^{65}Cu, ^{66}Zn, ^{67}Zn and ^{68}Zn) were collected using Faraday cups at positions L6, L4, L3, L2, Ax(C), H2 and H4, respectively, and all Faraday amplifiers used 10^{11} Ω resistors. Among them, the ^{60}Ni was used to monitor the interference of ^{64}Ni on ^{64}Zn. For all samples ^{64}Ni interference were negligible ($^{60}Ni/^{64}Zn < 5\times10^{-4}$). The samples were analyzed in low-resolution mode and a 300 ppb Zn solution returns ~4V for ^{64}Zn. Each analysis consisted of the integration of 25 cycles of 8 seconds each. Finally, zinc isotope ratios are reported in standard δ-notation in permil relative to JMC Lyon 3-0749L: $\delta^{X}Zn(‰) = [(^{X}Zn/^{64}Zn)_{sample}/(^{X}Zn/^{64}Zn)_{JMC\ Lyon\ 3\text{-}0749L} - 1] \times 1000$, where X = 66 and 68.

International standards and replicate analyses were applied to test the accuracy of the method.

Nine full replicates of these samples (dissolution from aliquots of a homogeneous powder, chemical purification and mass spectrometry measurements), show identical $\delta^{66}Zn$ values within the uncertainty of 0.05‰ (2sd). Full details of analytical procedures and standard samples have been reported in Zhu et al. (2019). The results of standard samples (Table S7) are consistent with previous studies and recommended values (Moynier et al., 2017) within error (0.05‰). The $\delta^{66}Zn$ and $\delta^{68}Zn$ values of all samples analyzed here fall onto a mass-dependent fractionation line with a slope of 1.9999 (Fig. S10).

References

Chen, S., Liu, Y., Hu, J., Zhang, Z., Hou, Z., Huang, F., Yu, H., 2016. Zinc Isotopic Compositions of NIST SRM 683 and Whole-Rock Reference Materials. Geostandards and Geoanalytical Research 40 (3) 417-432.

Gao, S., Rudnick, R.L., Yuan, H.-L., Liu, X.-M., Liu, Y.-S., Xu, W.-L., Ling, W.-L., Ayers, J., Wang, X.-C., Wang, Q.-H., 2004. Recycling lower continental crust in the North China craton. Nature 432 (7019) 892.

Liu, S.-A., Li, D., Li, S., Teng, F.-Z., Ke, S., He, Y., Lu, Y., 2014. High-precision copper and iron isotope analysis of igneous rock standards by MC-ICP-MS. J. Anal. At. Spectrom. 29 (1) 122-133.

Liu, Y., Zong, K., Kelemen, P.B., Gao, S., 2008. Geochemistry and magmatic history of eclogites and ultramafic rocks from the Chinese continental scientific drill hole: subduction and ultrahigh-pressure metamorphism of lower crustal cumulates. Chemical Geology 247 (1) 133-153.

Ma, Q., Zheng, J., Griffin, W.L., Zhang, M., Tang, H., Su, Y., Ping, X., 2012. Triassic “adakitic” rocks in an extensional setting (North China): melts from the cratonic lower crust. Lithos 149 159-173.

Maréchal, C.N., Télouk, P., Albarède, F., 1999. Precise analysis of copper and zinc isotopic compositions by plasma-source mass spectrometry. Chemical Geology 156 (1-4) 251-273.

Moynier, F., Vance, D., Fujii, T., Savage, P., 2017. The Isotope Geochemistry of Zinc and Copper. Reviews in Mineralogy and Geochemistry 82 (1) 543-600.

Zhu, Y.T., Li, M., Wang, Z.C., Zou, Z.Q., Hu, Z.C., Liu, Y.S., Zhou, L., Chai, X.N., 2019. High-precision Copper and Zinc Isotopic Measurements in Igneous Rock Standards Using Large-geometry MC-ICP-MS. Atomic Spectroscopy 40 (6) 206-214.

(4) Supplementary Text S2_Correction of the CO_2 effect on P-T estimates

Supplementary Text S2. Correction of CO_2 on P-T estimates

To correct the effect of CO_2 on P-T estimates with Lee et al's (2009) thermobarometer, we first used melt CaO vs. SiO_2 (Fig. S7a) to discriminate partial melts of carbonated source from CO_2-free source (Herzberg and Asimow, 2008). Most of the samples with SiO_2 > ~43 wt.% plot on the right side of the discriminating line, pointing to a CO_2-free mantle source. However, samples with SiO_2 < ~43 wt.% fall on the left side of the discriminating line, showing an affinity with a CO_2-bearing source. This observation means that calculated pressures for samples with SiO_2 < ~43 wt.% in Figure S7a were overestimated due to the presence of CO_2. We empirically corrected the pressures of these samples to fit the liner trend for samples with SiO_2 > ~43 wt.%, as defined by the blue line ($P = -0.2281 \times SiO_2 + 13.155$) in Figure S7b. The corrected results show that pressure was overestimated by 0.2-1.6 GPa for these samples. Following the pressure correction, we need to further correct the impact of CO_2 on temperature estimates. Because in carbonated peridotite system, melt CO_2 content is generally negatively correlated with melt SiO_2 contents. We therefore use the empirical equation of Dasgupta et al. (2013) to infer the melt CO_2 contents:

$$CO_2 = (44.8 - SiO_2)/0.89$$

We then correct the effect of CO_2 on melting temperature using the following empirical function:

$$\Delta T\ (°C) = a \times CO_2 + b \times \ln[(100 - c \times CO_2)/100]$$

Where a, b and c are pressure-dependent constants and are given in Dasgupta et al. (2013). Using this method, the average ΔT at 3-4 GPa (corrected pressure for samples with SiO_2 < ~43 wt.%) varies from 26 to 57 °C.

References

Dasgupta, R., Mallik, A., Tsuno, K., Withers, A.C., Hirth, G. and Hirschmann, M.M. (2013) Carbon-dioxide-rich silicate melt in the Earth's upper mantle. *Nature* **493**, 211-215.

Herzberg, C. and Asimow, P.D. (2008) Petrology of some oceanic island basalts: PRIMELT2. XLS software for primary magma calculation. *Geochem. Geophys. Geosyst.* **9**.

(5) Supplementary Text S3_Descriptions of mixing modelling in Fig. 4

Supplementary Text S3. Descriptions of mixing modeling in Fig. 4.

To produce carbonated eclogite with $\delta^{66}Zn$ as high as 0.45‰, we follow the method of Beunon et al. (2020) and assume that the carbonated eclogite is a mixture of 90% MORB-eclogite and 10% high-pressure carbonates. Because the solidus temperature of carbonated eclogite is significantly deeper and their melt productivity is higher than that of peridotites (Gerbode and Dasgupta, 2010), this component is expected to be completely molten when incipient melting (F=1%) of the surrounding peridotite matrix begins (Gerbode and Dasgupta, 2010). Therefore, we assume that, at the base of the melting column, low degree (F=1%) partial melts of peridotite are mixed with carbonated eclogites. The reaction of the carbonated eclogite-derived melt with surrounding peridotite should result into an increase of the orthopyroxene (opx) mode at the expense of olivine (Mallik and Dasgupta, 2014) and explain why "transitional lithologies" are predicted by the FCKANTMS parameter (see Fig. 6 in the manuscript).

The incipient melt composition of peridotite is calculated after Beunon et al. (2020). Our model shows that mixing this high-$\delta^{66}Zn$ carbonated eclogite component with less than 5% peridotite-derived low-degree melts can generate both the elevated Zn isotopes and the relatively enriched Sr-Nd isotopes of the low-silica samples (Fig. 4 in the manuscript). As upwelling progresses to shallower pressure, the melting degree enhances and the contribution of the depleted peridotite matrix increases, resulting in the dilution of the isotopically enriched component signal. Our model predicts the depleted endmember of the high-silica samples can be produced by mixing of 9-19% depleted peridotite mantle derived melt with carbonated eclogite melt at the deepest level of the melting column. This is consistent with the discussion that the low-silica samples, which contain less than 5% melt of matrix peridotite, is are more isotopically enriched compared to the depleted endmember of the high-silica samples.

During carbonated asthenosphere-lithosphere interaction, shallower silica-rich melts have significantly higher K/La, Ba/Th and Sr/Nd than the deeper melts, indicating a greater contribution from fossil subduction components. Here, we calculate the partial melt composition of isotopically enriched lithospheric mantle by assuming it was produced by mixing of melt from a more depleted peridotite residue with subducted sediment (GLOSS) (Plank and Langmuir, 1998) during earlier subduction events. The metasomatized depleted lithospheric mantle is assumed to be a F=15% partial melting residue of DMM, this residue was then metasomatized by GLOSS to account for

the isotopic compositions of enriched endmember of high-silica samples. Our isotopic modelling show that mixing of 7-9% subducted sediment (GLOSS) to partial melts of sub-continental lithospheric mantle can produce the enriched component of the high-silica samples. If we assume a more fertile lithospheric mantle residue, e.g., similar to melting residue of the asthenosphere with an extremely low melting degree of 1%, a much higher proportion of GLOSS (20-27%) would be required to account for the enriched endmember of high-silica samples and the observed negative correlation between $\delta^{66}Zn$ and Sr isotopes and the positive correlation between $\delta^{66}Zn$ and Nd isotopes.

Parameters used for model calculation

	Carbonate[a]	Eclogite[b]	Carbonated eclogite[c]	Melt of asthenospheric peridotite[d]	Melts of depleted lithospheric residue before subduction modification[e]	GLOSS[f]
Sr (ppm)	1.84	180	162	530	122	327
$^{87}Sr/^{86}Sr$	0.7164	0.7039	0.703914	0.70219	0.70219	0.7173
Nd (ppm)	0.1	7.3	6.58	21	6.67	27
$^{143}Nd/^{144}Nd$	0.51214	0.51288	0.512879	0.51318	0.51318	0.512182
Zn (ppm)	280	80	100	78	73.1	86.4
$\delta^{66}Zn$	0.91	0.27	0.4492	0.23	0.22	0.28

[a] Carbonate is from Jin et al. (2020).

[b] Eclogite: Sr and $^{87}Sr/^{86}Sr$ is from Hauff et al. (2003), the same value as used in Li and Wang (2018) and this corresponds to the most sea-water altered basalt drilled on the ocean crust closed to the Mariana trench. Nd is from Jin et al. (2020). $^{143}Nd/^{144}Nd$ is from Cousens (1992). Zn and $\delta^{66}Zn$ is from Jin et al. (2020).

[c] Carbonated eclogite is assumed to be mixture of 90% eclogite with 10% carbonate, after Beunon et al. (2020).

[d] Melt of asthenospheric peridotite is assumed to be low-degree melt (F=1%) of DMM. Sr-Nd-Zn contents and $\delta^{66}Zn$ is from Beunon et al. (2020), $^{87}Sr/^{86}Sr$ and $^{143}Nd/^{144}Nd$ is from Workman and Hart (2005).

[e] Melt of depleted lithospheric residue before subduction modification is assumed to be high-degree melting residue (F=15%) of DMM. $^{87}Sr/^{86}Sr$ and $^{143}Nd/^{144}Nd$ ~~is~~ are from Workman and Hart (2005), Sr, Nd, Zn and $\delta^{66}Zn$ is calculated following Beunon et al. (2020).

[f] GLOSS: Zn-Sr-Nd contents and Sr-Nd isotopic composition is from Plank and Langmuir (1998) and $\delta^{66}Zn$ is from Moynier et al. (2017).

References

Beunon, H., Mattielli, N., Doucet, L.S., Moine, B., Debret, B., 2020. Mantle heterogeneity through Zn systematics in oceanic basalts: Evidence for a deep carbon cycling. Earth-Science Reviews 205.

Cousens, B., 1992. A Pb, Sr and Nd isotopic study of basaltic rocks from the Sea of Japan, Legs, 127/128. Proceedings of the Ocean Drilling Program, Scientific Results 127 805-817.

Gerbode, C., Dasgupta, R., 2010. Carbonate-fluxed melting of MORB-like pyroxenite at 2· 9 GPa and genesis of HIMU ocean island basalts. Journal of Petrology 51 (10) 2067-2088.

Hauff, F., Hoernle, K., Schmidt, A., 2003. Sr-Nd-Pb composition of Mesozoic Pacific oceanic crust (Site 1149 and 801, ODP Leg 185): Implications for alteration of ocean crust and the input into the Izu-Bonin-Mariana subduction system. Geochemistry, Geophysics, Geosystems 4 (8).

Jin, Q.-Z., Huang, J., Liu, S.-C., Huang, F., 2020. Magnesium and zinc isotope evidence for recycled sediments and oceanic crust in the mantle sources of continental basalts from eastern China. Lithos 370-371.

Li, S., Wang, Y.J.S.C.E.S., 2018. Formation time of the big mantle wedge beneath eastern China and a new lithospheric thinning mechanism of the North China craton—Geodynamic effects of deep recycled carbon. 1-16.

Mallik, A., Dasgupta, R., 2014. Effect of variable CO2 on eclogite‐derived andesite and lherzolite reaction at 3 GPa—Implications for mantle source characteristics of alkalic ocean island basalts. Geochemistry, Geophysics, Geosystems 15 (4) 1533-1557.

Moynier, F., Vance, D., Fujii, T., Savage, P., 2017. The isotope geochemistry of zinc and copper. Reviews in Mineralogy and Geochemistry 82 (1) 543-600.

Plank, T., Langmuir, C.H., 1998. The chemical composition of subducting sediment and its consequences for the crust and mantle. Chemical geology 145 (3) 325-394.

Workman, R.K., Hart, S.R., 2005. Major and trace element composition of the depleted MORB mantle (DMM). Earth and Planetary Science Letters 231 (1-2) 53-72.